

# *Observations of the chemical and thermal response of 'ring rain' on Saturn's ionosphere*

Article

Accepted Version

O'Donoghue, J. ORCID: <https://orcid.org/0000-0002-4218-1191>, Moore, L., Connerney, J., Melin, H., Stallard, T. S., Miller, S. and Baines, K. H. (2019) Observations of the chemical and thermal response of 'ring rain' on Saturn's ionosphere. *Icarus*, 322. pp. 251-260. ISSN 0019-1035 doi: 10.1016/j.icarus.2018.10.027 Available at <https://centaur.reading.ac.uk/120084/>

It is advisable to refer to the publisher's version if you intend to cite from the work. See [Guidance on citing](#).

To link to this article DOI: <http://dx.doi.org/10.1016/j.icarus.2018.10.027>

Publisher: Elsevier

All outputs in CentAUR are protected by Intellectual Property Rights law, including copyright law. Copyright and IPR is retained by the creators or other copyright holders. Terms and conditions for use of this material are defined in the [End User Agreement](#).

[www.reading.ac.uk/centaur](http://www.reading.ac.uk/centaur)

**CentAUR**

Central Archive at the University of Reading

Reading's research outputs online

# 1 Observations of the chemical and thermal response of 2 ‘ring rain’ on Saturn’s ionosphere

3 James O’Donoghue<sup>a</sup>, Luke Moore<sup>b</sup>, Jack Connerney<sup>c,a</sup>, Henrik Melin<sup>d</sup>, Tom  
4 Stallard<sup>d</sup>, Steve Miller<sup>e</sup>, Kevin H. Baines<sup>f</sup>

5 <sup>a</sup>*Planetary Magnetospheres Laboratory, NASA Goddard Space Flight Center, Greenbelt,*  
6 *Maryland, USA*

7 <sup>b</sup>*Center for Space Physics, Boston University, Massachusetts, USA*

8 <sup>c</sup>*Space Research Corporation, Annapolis, Maryland, USA*

9 <sup>d</sup>*Department of Physics and Astronomy, University of Leicester, Leicester, UK*

10 <sup>e</sup>*Atmospheric Physics Laboratory, Department of Physics and Astronomy, University*  
11 *College London, London, WC1E 6BT, UK*

12 <sup>f</sup>*NASA Jet Propulsion Laboratory, M/S 183-601, 4800 Oak Grove Drive, Pasadena, CA*  
13 *91109, USA*

---

## 14 Abstract

In this study we performed a new analysis of ground-based observations that were taken on 17 April 2011 using the 10-metre Keck telescope on Mauna Kea, Hawaii. Emissions from  $\text{H}_3^+$ , a major ion in Saturn’s ionosphere, were previously analyzed from these observations, indicating that peaks in emission at specific latitudes were consistent with an influx of charged water products from the rings known as ‘ring rain’. Subsequent modeling showed that these peaks in emission are best explained by an increase in  $\text{H}_3^+$  density, rather than in column-averaged  $\text{H}_3^+$  temperatures, as a local reduction in electron density (due to charge exchange with water) lengthens the lifetime of  $\text{H}_3^+$ . However, what has been missing until now is a direct derivation of the  $\text{H}_3^+$  parameters temperature, density and radiative cooling rates, which are required to confirm and expand on existing models and theory. Here we present measurements of these  $\text{H}_3^+$  parameters for the first time in the non-auroral regions of Saturn, using two  $\text{H}_3^+$  lines, Q(1,0<sup>-</sup>) and R(2,2). We confirm that  $\text{H}_3^+$  density is enhanced near the expected ‘ring rain’ planetocentric latitudes near 45°N and 39°S. A low  $\text{H}_3^+$  density near 31°S, an expected prodigious source of water, may indicate that the rings are ‘overflowing’ material into the planet such that  $\text{H}_3^+$  destruction by charge-exchange with incoming neutrals outweighs its lengthened lifetime due to the aforementioned reduction

in electron density. Derived  $\text{H}_3^+$  temperatures were low while the density was high at  $39^\circ\text{S}$ , potentially indicating that the ionosphere is most affected by ring rain in the deep ionosphere. Saturn’s moon Enceladus, a known water source, is connected with a dense region of  $\text{H}_3^+$  centered on  $62^\circ\text{S}$ , perhaps indicating that charged water from Enceladus is draining into Saturn’s southern mid-latitudes. We estimated the water product influx using previous modeling results, finding that  $432 - 2870 \text{ kg s}^{-1}$  of water delivered to Saturn’s mid-latitudes is sufficient to explain the observed  $\text{H}_3^+$  densities. When considering this mechanism alone, Saturn will lose its rings in  $292^{+818}_{-124}$  million years.

15 *Keywords:* Saturn, ionosphere, rings, magnetosphere, ring rain

---

## 16 1. Introduction

17 In the Saturn system, submicrometre charged icy grains are able to stream  
18 from the rings into the planetary atmosphere via the magnetic field. This  
19 process, termed “ring rain”, erodes and sculpts the ring system through  
20 the interplay between electromagnetic, gravitational and centrifugal forces  
21 (Northrop and Hill, 1982; Connerney, 2013). Saturn’s atmosphere adopts  
22 this discarded ring matter, causing dramatic changes in ionospheric chem-  
23 istry and the removal of haze (O’Donoghue et al., 2013; Connerney, 1986).  
24 Saturn’s ring system is comprised of clusters of ice ranging in size from be-  
25 low 0.01 cm and up to 10 m distributed in an approximately inverse cubic  
26 power-law manner, such that the majority of ring system is composed of small  
27 fragments (Zebker et al., 1985; Cuzzi et al., 2009). The chemical composition  
28 of the rings is considered to be almost pure water ice, but they are thought to  
29 be contaminated by tholins - a mixture of simple hydrocarbons (e.g.  $\text{CH}_4$  and  
30  $\text{C}_2\text{H}_6$ ), nitrogen and other components, giving the rings their characteristic  
31 tan color (Nicholson et al., 2008; Cuzzi et al., 2018). Submicrometre-sized ice  
32 particles or icy grains are able to acquire charge via photoionization or ex-  
33 posure to a micrometeorite impact’s dense plasma cloud (Connerney, 2013).  
34 On becoming charged, these grains have an array of velocities with respect to  
35 the planetary magnetic field which permeates the rings: this is either faster  
36 (super-rotating), slower (sub-corotating) or the same velocity as the moving  
37 magnetic field lines, which rotate at the solid-body planetary rotation rate.

38  
39 Three major forces act on the charged grains in Saturn’s rings **along a**

40 given magnetic field line: gravity pulling the grains towards the planet, and  
 41 the centrifugal and magnetic mirror forces which act to pull the grains back  
 42 into the ring plane. At  $1.62 R_S$  (where  $1 R_S$  is Saturn's equatorial radius  
 43 60,268 km) within the ring plane, charged grains that are stationary with  
 44 respect to the magnetic field experience only gravitational and centrifugal  
 45 forces, which are in balance at this location (the grain is stable) (Northrop  
 46 and Hill, 1982). At radial distances slightly less than  $1.62 R_S$ , however, grav-  
 47 ity begins to dominate, accelerating charged grains towards the planet (the  
 48 grain is unstable) (Northrop and Hill, 1983). However, charged grains mov-  
 49 ing at Keplerian velocity super-rotate with respect to the magnetic field and  
 50 therefore orbit magnetic field lines due to the Lorentz force. These grains,  
 51 unlike those at  $1.62 R_S$ , are subjected to a magnetic mirror force which re-  
 52 pels them back towards the ring plane when they approach the planet; this  
 53 breed of grain therefore has a radius of force balance that is closer to Saturn,  
 54 which is calculated to be  $1.525 R_S$  (Northrop and Hill, 1983; Northrop and  
 55 Connerney, 1987; Connerney, 2013). The sharp density gradient between the  
 56 B and C rings is near  $1.525 R_S$ , and may even be the result of 'ring rain' elec-  
 57 tromagnetically eroding the rings at this location (Northrop and Connerney,  
 58 1987).

59  
 60 Saturn's magnetic dip equator lies above the ring plane offset towards  
 61 Saturn's north pole, so that near to the ring plane the magnetic field has a  
 62 component pointing towards the southern hemisphere. As a result, at radial  
 63 distances  $< 1.525 R_S$ , recently produced ionized grains that are relatively  
 64 motionless compared to the rings will be drawn southwards; gravitational  
 65 forces acting parallel to magnetic field lines are in control here. Note that  
 66 the grains also have a perpendicular (to the ring plane) velocity distribution  
 67 of their own which pushes them either northwards or southwards; assuming  
 68 this is a Maxwellian-like distribution, the grains will still preferentially be  
 69 drawn southwards, with only the highest velocity grains potentially able to  
 70 escape northwards. Charged grains produced between  $1.525 R_S$  and  $1.62 R_S$   
 71 also fall preferentially to the south, but the grains are able to oscillate about  
 72 the ring plane here due to the weaker gravitational force pulling the grains  
 73 planetward along field lines (Connerney, 1986). Pathways for an influx of  
 74 ring material into the equatorial ionosphere have also been modeled. For  
 75 example, collisional drag may explain the influx of neutral grains (Mitchell  
 76 et al., 2018), whereas positively charged dust grains are also expected to be  
 77 deposited near Saturn's equator (Liu and Ip, 2014; Hsu et al., 2018). Such in-

fluxes, which have now been observed by Cassini (Mitchell et al., 2018; Perry et al., 2018; Hsu et al., 2018; Waite et al., 2018), would help to explain the observed depletion in ionospheric electron density there (Kliore et al., 2014). Estimating the mass loss of the rings is of great importance for determining the age, lifetime and evolution of the rings, which are presently understood to have existed for between 4.4 million and 4.5 billion years (see Northrop and Connerney, 1987; Connerney, 2013, and references therein).

The Pioneer 11 spacecraft was the first human made object to fly by Saturn in 1979 (Kliore et al., 1980). Saturn’s ionosphere was predicted to have an electron density of around  $10^5 \text{ cm}^{-3}$ , based on photoionization of atmospheric neutrals (mostly H and H<sub>2</sub>) by extreme ultraviolet (EUV) radiation from the Sun (McElroy, 1973; Waite et al., 1979). However, when Kliore et al. (1980) analyzed the attenuation of the Pioneer 11 radio signal, which had traveled through Saturn’s ionosphere, the electron density peak was found to be  $\sim 10^4 \text{ cm}^{-3}$ , an order of magnitude lower than predicted. Later, the Voyager 1 and 2 spacecraft, in 1980 and 1981 respectively, showed peak electron densities between  $\sim 6 \times 10^3 \text{ cm}^{-3}$  and  $\sim 2.3 \times 10^4 \text{ cm}^{-3}$  (Atreya et al., 1984). The lowest electron densities were found at  $36^\circ$  north, while the highest densities were found at  $73^\circ$  north: this was counter-intuitive since the electron production mechanism is solar EUV ionization, which is maximized at mid-to-low latitude, depending on season. These model-observation discrepancies could be resolved however, with the introduction of a planet-wide exogenous water influx of  $\sim 4 \times 10^7 \text{ molecules cm}^{-2} \text{ s}^{-1}$ , which leads to a net reduction in electron density (Connerney and Waite, 1984; Moses and Bass, 2000). In addition, a localized water influx of  $\sim 2 \times 10^9 \text{ molecules cm}^{-2} \text{ s}^{-1}$  was predicted to fall into Saturn from the inner edge of the B ring (at  $\sim 1.525 R_S$ ) (Connerney and Waite, 1984). The Cassini spacecraft later revealed latitudinal variations of peak electron densities using 59 radio occultations, with values ranging from  $\sim 1 \times 10^3 \text{ cm}^{-3}$  to  $\sim 3 \times 10^4 \text{ cm}^{-3}$  which correspond to the low-mid latitudes and auroral regions, respectively (Kliore et al., 2014).

Observations consistent with a ring-derived water influx that flows along magnetic field lines were first found using Voyager 2 green filter images of Saturn by Connerney (1986), which showed dark bands (indicating less reflection of sunlight) at  $44^\circ$ ,  $46^\circ$ ,  $52^\circ$  and  $64^\circ$  planetocentric latitude north. These bands map along magnetic field lines to  $1.525 R_S$ ,  $1.62 R_S$ ,  $1.95 R_S$  and  $3.95 R_S$ , respectively, in the ring plane. The first two listed radial dis-

116 tances correspond to the theoretical water sources between the B and C rings  
 117 discussed earlier, while 1.95  $R_S$  corresponds to the Cassini division, and 3.95  
 118  $R_S$  is the orbit of Enceladus - a known source of water to the Saturnian mag-  
 119 netosphere (Dougherty et al., 2006; Hansen et al., 2011). The reduction in  
 120 reflected light leading to these dark bands is thought to indicate the loss of  
 121 stratospheric haze: Connerney (1986) proposed that haze particles could act  
 122 as condensation nuclei to the downward diffusing water, thus making haze  
 123 particles heavy enough to sink. Saturn's hydrocarbon (e.g.  $C_2H_2$ ) abundance  
 124 was calculated at four latitudes using Hubble Space Telescope (HST) obser-  
 125 vations, with a minimum value found at  $41^\circ$  south while increasing towards  
 126 the polar regions (Prangé et al., 2006). As photochemical models show that  
 127 the presence of water in the stratosphere depletes hydrocarbons (Moses and  
 128 Bass, 2000), the results were described by Prangé et al. (2006) to be con-  
 129 sistent with an influx of water flowing from the rings to the atmosphere via  
 130 magnetic field lines.

131

132  $H_3^+$ , one of the most abundant ions in Saturn's ionosphere, is produced  
 133 in the following reaction chain:



134 Where  $e^*$  is a fast electron and EUV is an extreme ultraviolet photon  
 135 from the Sun. As soon as  $H_2^+$  is created by reactions (1) - (3), reaction (4)  
 136 takes place almost instantaneously (Miller et al., 2010; Stallard et al., 2015).  
 137 In the auroral/polar region,  $H_3^+$  peaks in density at an altitude of  $\sim 1155$   
 138 km above the 1-bar pressure surface (Stallard et al., 2012), and production  
 139 occurs in the range 900 to 4000 km (Tao et al., 2011).

140

141 In 2011, the 10 meter Keck II telescope on Mauna Kea, Hawaii, was used  
 142 to observe the pole-to-pole  $H_3^+$  ion emissions from Saturn (O'Donoghue et al.,  
 143 2013). Broad peaks in  $H_3^+$  intensity were discovered at planetocentric lati-  
 144 tudes  $43^\circ$  and  $38^\circ$  north and south, respectively. As a result of the geometry  
 145 of Saturn's magnetic field, which can be thought of as being approximated  
 146 by a dipole that is slightly offset north of the planet's center, both latitudes  
 147 share a common field line; this field line intersects the ring plane at  $\sim 1.525$

148  $R_S$  (Connerney, 1986). Magnetic conjugacy was directly observed, so the  
 149 intensity peaks that were found are related to the magnetosphere. Following  
 150 this observation, Moore et al. (2015) demonstrated through modeling that  
 151 the increase in  $H_3^+$  emissions was better explained via an increase in  $H_3^+$  den-  
 152 sity, rather than a (column-averaged)  $H_3^+$  temperature increase. It was found  
 153 that any water product inflow under  $1 \times 10^7$  molecules  $\text{cm}^{-2} \text{s}^{-1}$  will rapidly  
 154 recombine with electrons, mitigating the loss of  $H_3^+$  by the same process,  
 155 such that  $H_3^+$  densities ought to be larger where water falls. However, Moore  
 156 et al. (2015) also found that for large water influxes (greater than  $\sim 2 \times 10^8$   
 157 molecules  $\text{cm}^{-2} \text{s}^{-1}$ ) the loss rate of  $H_3^+$  by charge-exchange with water be-  
 158 gins to overtake the enhancement in  $H_3^+$  by the reduction in electron density.  
 159

160 More recently, the signature of ring rain in  $H_3^+$  emissions were re-detected  
 161 in Keck II telescope observations taken in 2013; the brightness of these emis-  
 162 sions was a factor of  $\sim 4$  lower than in 2011, likely owing to an estimated 90 K  
 163 decrease in ionospheric temperature from 2011 to 2013 (O'Donoghue et al.,  
 164 2017). Surprisingly however, the contrast between bright and dim features  
 165 in  $H_3^+$  emissions were larger in 2013, indicating an increased influx of ring  
 166 material. Indeed, because the opening angle of the rings was larger in 2013,  
 167 more of the ring's surface area is exposed to solar EUV ionization, so the pro-  
 168 duction of charged icy grains ought to be larger (O'Donoghue et al., 2017).  
 169 In 2017 the Cassini spacecraft flew between the planet and rings, allowing for  
 170 the first time the ability to probe the ring-planet interface region in situ. On-  
 171 board Cassini, the impact mass spectrometer Cosmic Dust Analyzer (CDA;  
 172 Srama et al. (2004)), detected the presence of grains tens of nanometers in  
 173 size at high concentration near the ring plane and at mid-latitudes in the  
 174 northern and southern hemispheres: a spectacular confirmation of the ring  
 175 rain process (Hsu et al., 2018). In the present paper we continue to expand  
 176 our understanding of ring-atmosphere coupling by assessing the thermal and  
 177 chemical influence ring rain has on Saturn's ionosphere for the first time,  
 178 through a new analysis of Keck II data taken in 2011 (O'Donoghue et al.,  
 179 2013).

## 180 **2. Observations and data reduction**

181 Ground-based observations of Saturn were obtained on 17 April 2011, be-  
 182 tween 10:33:42 and 12:46:28 Universal Time (UT), using the 10-metre Keck  
 183 telescope on Mauna Kea, Hawaii. The dataset obtained in this observation



184 is available in the linked Research data. Saturn’s northern hemisphere was  
 185 tilted towards the Earth (and the Sun) with a sub-Earth latitude of  $8.2^\circ$  -  
 186 Saturn was in northern spring. The collected light was passed to the high-  
 187 resolution Near-InfraRed SPECTrometer, NIRSPEC (McLean et al., 1998),  
 188 which was used in cross-dispersed mode with a resolution of  $R = \lambda/\Delta\lambda$   
 189  $\sim 25,000$ , providing a spectral resolution of  $\Delta\lambda \approx 1.59 \times 10^{-4} \mu\text{m}$  at  $3.975$   
 190  $\mu\text{m}$ . The wavelengths covered were near  $3.5$  and  $4.0 \mu\text{m}$ , as they include the  
 191 Q- and R-Branch ro-vibrational transition lines of the  $\text{H}_3^+$  ion. NIRSPEC’s  
 192 slit dimensions were configured to be  $0.432''$  wide by  $24''$  long, with a pixel on  
 193 the CCD corresponding to  $0.144''$  squared on the sky. The spectrometer slit  
 194 was aligned along Saturn’s noon meridian in a north-south direction, along  
 195 the axis of the planet’s rotation as shown in Figure 1. Note that Saturn’s  
 196 magnetic field is co-aligned with the planetary axis of rotation to  $0.0095^\circ$   
 197 (Dougherty et al., 2018). While the planet rotated, spectral images were  
 198 acquired of Saturn between  $103 - 176^\circ$  Saturn System III Central Meridian  
 199 Longitude (CML). Each set of spectra acquired consists of twelve 5-s inte-  
 200 grations, creating exposures 60 s long, consisting of Saturn (A) and sky (B)  
 201 frames with the telescope slewing between the relevant positions of each in  
 202 the sky in an ABBA pattern: in total, 46 A and 46 B frames were captured.

203 Standard astronomical data reduction techniques were applied to the  
 204 data, such as sky subtraction, accounting for non-uniformity in the response  
 205 of NIRSPEC’s detector and flux calibration (using the star HR 6035). These  
 206 processes ensure that unwanted emissions from Earth’s atmosphere (mainly  
 207 from water), telescope and instruments are removed, and that photon counts  
 208 at the detector are converted to units of physical flux - see e.g. O’Donoghue  
 209 et al. (2016) for more details. After data reduction, each spectral image  
 210 is aligned before being co-added to produce a single image representing the  
 211 entire dataset, selected wavelengths of which are shown in Figure 2. Using ge-  
 212 ometric information obtained from planetary ephemeris (NASA’s Horizons  
 213 web interface at <https://ssd.jpl.nasa.gov/horizons.cgi>), planetocentric lati-  
 214 tudes were assigned to the data. Telluric seeing, which during this period  
 215 was  $\sim 0.4''$ , adds uncertainty in determining the location of the planet’s limbs  
 216 since the data are spatially smeared by  $\pm 2$  pixels, equating to  $\sim 2$  of latitude  
 217 near  $45^\circ$  north. A cosine correction of the planetary emission angle was ap-  
 218 plied to remove the line-of-sight effects of viewing geometry.

219  
 220 One of the challenges of this work is measuring  $\text{H}_3^+$  transition line emis-  
 221 sions at mid-to-low latitudes, which are up to an order of magnitude weaker

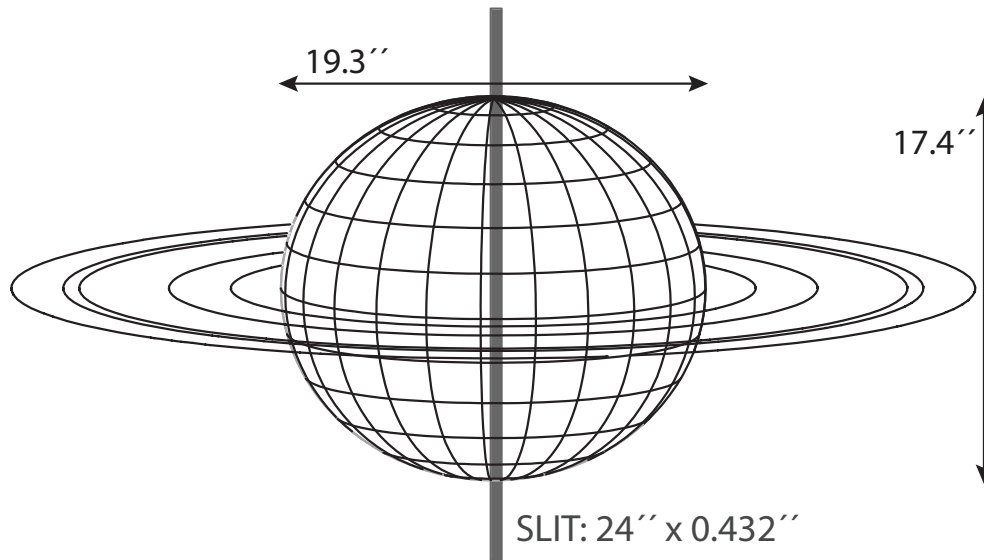


Figure 1: Saturn in conditions of northern spring, 17 April 2011. Gridlines on the planetary body are spaced in 15-degree intervals of longitude and latitude. The arrowed lines show the angular extent of Saturn and the dimensions of the NIRSPEC spectral slit in seconds of arc. This image was generated using the Planetary Data System (PDS) online tools at <https://pds-rings.seti.org/tools/>.

222 than auroral/polar emissions at Saturn.  $\text{H}_3^+$  emissions are therefore more  
 223 sensitive to residual signals left over from the data reduction process, e.g.  
 224 sky emission subtraction leaves residuals of about 1% of the peak auroral  
 225 intensity, which is about 1-10% of the peak intensity at mid-to-low latitudes.  
 226 This is mitigated against by selecting larger spatial areas (longitude and lat-  
 227 itude) in order to increase the signal to noise. The next challenge is in how  
 228 to deal with unwanted emissions emanating from Saturn itself, which has  
 229 at least over 100 different species of neutrals and ions present (Moses and  
 230 Bass, 2000); the emissions wavelengths from many of the lower-abundance  
 231 members of these species are not fully understood, and so may register as  
 232 localized noise at specific wavelengths and latitudes. The two  $\text{H}_3^+$  lines in  
 233 this study, however, were chosen in Kronian-atmospheric windows produced  
 234 by methane's absorption of sunlight, avoiding noisy regions at most lati-  
 235 tude seen on the left of panel b) in Figure 2. Previous studies have been  
 236 successful in deriving  $\text{H}_3^+$  temperatures and densities from two  $\text{H}_3^+$  spectral  
 237 lines (O'Donoghue et al., 2016; Johnson et al., 2018). Figure 3 shows the  
 238 co-addition of data from Figure 2 between  $30^\circ$  to  $39^\circ$  planetocentric latitude

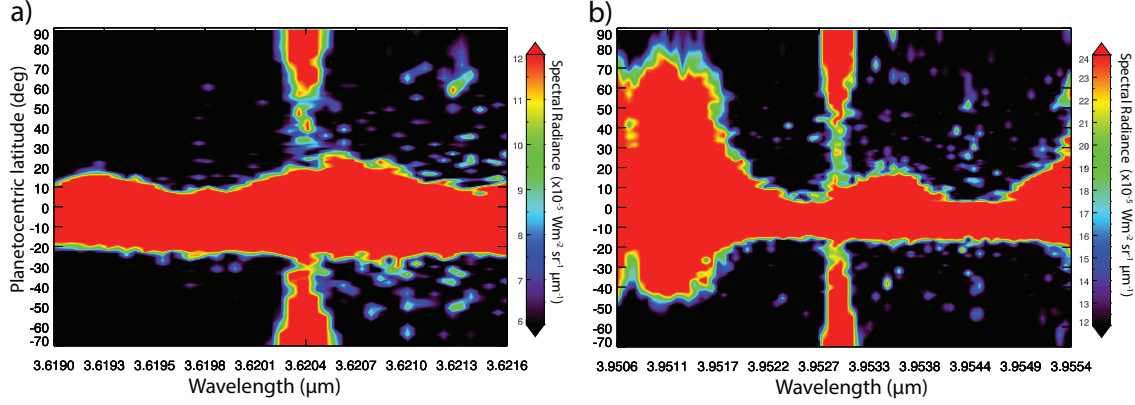


Figure 2: Fully reduced co-added spectrum composed of 46 spectral images of Saturn, in wavelength and planetocentric latitude. These two panels are centered on two (vertical) ro-vibrational transition lines of  $\text{H}_3^+$ . In a) is the R-branch  $\text{H}_3^+$  transition line designated R(2,2<sup>-</sup>), while b) shows the fundamental  $\text{H}_3^+$  line, Q(1,0<sup>-</sup>). Both lines are observable because methane absorbs most of the incident solar radiation in these wavelength ranges. The horizontal emissions near the equator are the continuum reflection of sunlight from the rings. Note that the spectral radiance is ‘thresholded’ between the numbers shown in the color bars.

239 south. Fitting to  $\text{H}_3^+$  lines (described in the Data Analysis section) requires  
 240 that the minimum background spectral radiance is found and subtracted, so  
 241 that the  $\text{H}_3^+$  line begins from a background of zero. Pixel-to-pixel extremes,  
 242 such as hot pixels that survived the data reduction process, were accounted  
 243 for by smoothing the data by  $0.0025 \mu\text{m}$  (4 pixels) prior to establishing the  
 244 minima of each bin. Figure 3 displays a background subtraction as shifted  
 245 data (black asterisks), with the pre-shifted data in grey.

246  
 247 To remove unwanted, blended emissions from the  $\text{H}_3^+$  lines (shown in red  
 248 in Figure 3 and labeled as noise), a non-linear least squares curve fitting rou-  
 249 tine called MPFIT was employed (Markwardt, 2009). In this work, MPFIT  
 250 is programmed to look for multiple Gaussians within the data; the first Gaus-  
 251 sian distribution is fixed in wavelength to an  $\text{H}_3^+$  line and allowed to vary in  
 252 height and width, while additional Gaussians are used to characterize nearby  
 253 noise and are free to vary in wavelength, height and width. Typically each  
 254  $\text{H}_3^+$  line is either not blended or is blended with one other line, as is the case  
 255 in Figure 3). Once a solution is found, the Gaussian noise distributions are  
 256 subtracted from the data, leading to the gold colored  $\text{H}_3^+$ -only line in Figure

257 3.

258 Standard deviations in the Q-and R- branch data were calculated from  
259 the wavelength ranges 3.954 - 3.955  $\mu\text{m}$  and 3.618 - 3.62  $\mu\text{m}$ , respectively,  
260 and included the planetocentric latitude range 40° to 90°N. These areas were  
261 chosen to represent the standard deviation, rather than the area immedi-  
262 ately around the  $\text{H}_3^+$  lines, in order to accurately represent the dispersion  
263 of data in the array: the standard deviation is thus less affected by small  
264 spatial/spectral scale features, such as residuals leftover from sky subtraction  
265 and uncharacterized emissions from Saturn’s many species. When estimating  
266 the minimum background of the smoothed array for the purposes of shifting  
267 the array down, an additional uncertainty is introduced: this is included by  
268 calculating the standard deviation of the smoothed array in the latitude and  
269 wavelength ranges above. A final uncertainty is introduced after using MP-  
270 FIT - the model-data difference known as residuals. These residuals, along  
271 with the standard deviations above, are propagated through to achieve the  
272 final standard deviations shown in Figure 3. Note that the Q-branch data  
273 are a factor  $\sim 3$  brighter than the R-branch, so three standard deviations are  
274 shown in this figure instead of one for aesthetic purposes.

### 276 3. Data analysis

277  $\text{H}_3^+$  emits a spectrum of at least 3 million ro-vibrational transition lines,  
278 and each line varies in intensity at a particular rate that depends on the  
279 ion’s temperature (Neale et al., 1996). With a model of this temperature  
280 dependence we can therefore obtain the column-averaged  $\text{H}_3^+$  temperature,  
281  $T_{\text{H}_3^+}$  (Kelvin), through observations of the ratio between two or more  $\text{H}_3^+$   
282 emission lines. The model fitting routine used herein uses the spectroscopic  
283 line list from Neale et al. (1996), the latest  $\text{H}_3^+$  partition function constants  
284 from Miller et al. (2010), and varies a sum of Gaussian distributions that  
285 represent  $\text{H}_3^+$  (called the spectral function) until the line-ratios match the  
286 least squares fit to the observed data (for more detail see Melin et al., 2013,  
287 and references therein). To find the total number of emitting ions per unit  
288 area - the  $\text{H}_3^+$  column density - we divide the observed emissions by those  
289 that a single  $\text{H}_3^+$  ion emits at the temperature calculated above. This pro-  
290 duces a column-integrated density,  $N_{\text{H}_3^+}$  ( $\text{cm}^{-2}$ ). The radiative cooling rate  
291 (or, radiance) of  $\text{H}_3^+$  is given by  $L_{\text{H}_3^+}$  ( $\text{Wm}^{-2} \text{sr}^{-1}$ ): it is the radiative power  
292 imparted by  $\text{H}_3^+$  at all wavelengths from a surface area to a given steradian

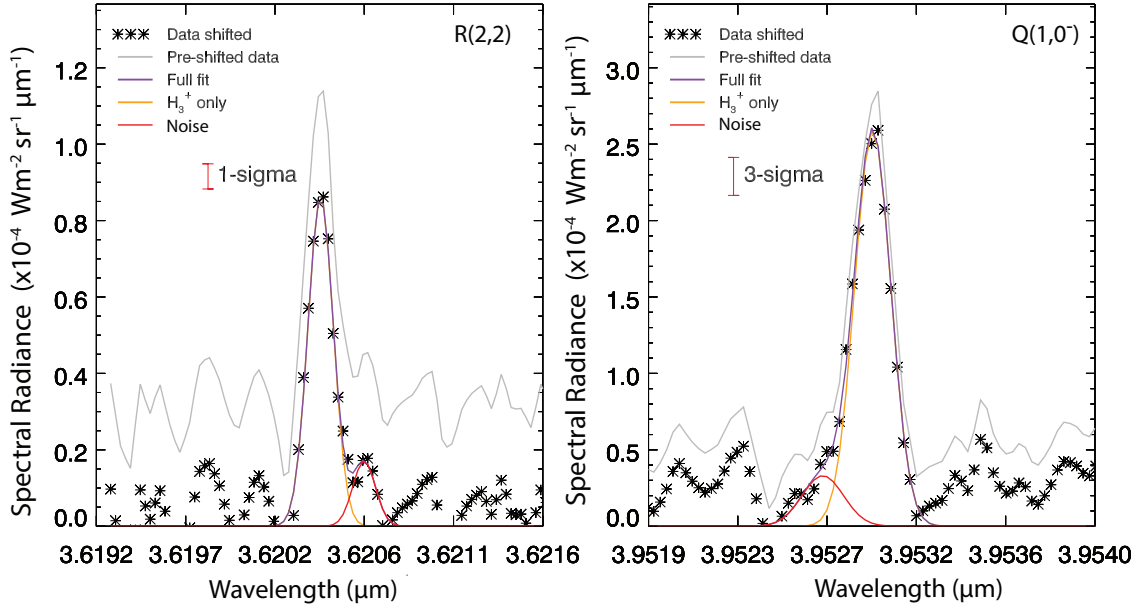


Figure 3: Spectral radiance of Saturn co-added from 103 - 176° CML and 37 - 47°S planetocentric latitude, extracted from the data presented in Figure 2. A full description of the features of this figure is given in the main text.

of solid angle. Calculation of  $L_{H_3^+}$  is achieved by multiplying  $N_{H_3^+}$  by the sum of all emissions of a single  $H_3^+$  ion for the calculated  $T_{H_3^+}$ . The radiative cooling rate was introduced by Lam et al. (1997) as ‘total emission’ in a study of Jupiter’s ionospheric  $H_3^+$ .  $L_{H_3^+}$  is a useful parameter as it reveals the amount of energy lost by the ionosphere via radiative cooling to space by  $H_3^+$ .

Prior to fitting to data using the above  $H_3^+$  model, the  $H_3^+$ -only emissions and a single standard deviation from Figure 3 are extracted. In Figure 4, modified  $H_3^+$ -only line emissions from Figure 3 are shown, with each new data curve representing an original  $H_3^+$ -only curve, but with the addition and subtraction of one standard deviation from each respective panel. The  $H_3^+$ -fitting model is then run as follows: first, the lower data curve from panel a) is fitted alongside the higher data curve in panel b) and second, the higher data curve from panel a) is fitted with the lower data curve of panel b). Performing the fits this way ensures that the full range of possible line ratios between these two  $H_3^+$  lines are included in the results, based on the relative standard deviations from each panel. Having a range of possible fits

310 leads to a range of  $H_3^+$  parameter outputs ( $T_{H_3^+}$ ,  $N_{H_3^+}$ ,  $L_{H_3^+}$ ): the upper and  
 311 lower values for each parameter, along with the uncertainties from the model  
 312 fitting itself, represent the overall uncertainties in the results to follow. Note  
 313 that the data in Figure 4 rests on random noise that was generated within  
 314 the bounds of one standard deviation, and that this used to illustrate the  
 315 uncertainty in background of the array.

316

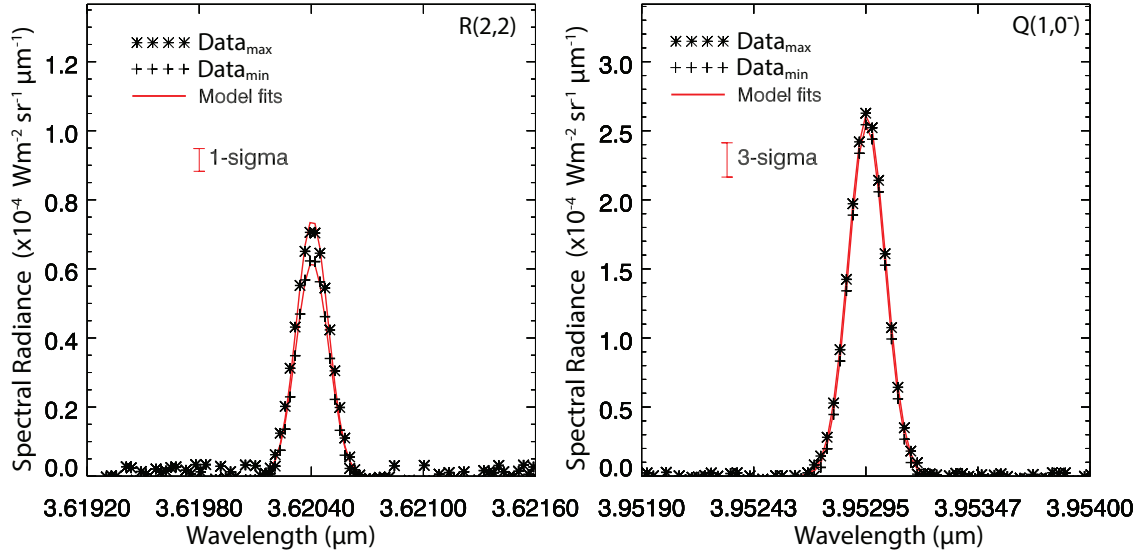


Figure 4: As Figure 3, but only including a modified version of  $H_3^+$ -only emissions and model fits to the data, as described in the main text.

317 In order to map planetary latitudes to radial distance in the ring plane,  
 318 the path of magnetic field lines are traced from the ionosphere to the ring  
 319 plane using a model of Saturn's magnetosphere. For this, we use the Voy-  
 320 ager 2 "Z3" magnetic mapping model of Connerney et al. (1982) with the  
 321 coefficients:  $g_1 = 21,248 \text{ nT}$ ,  $g_2 = 1,613$ ,  $g_3 = 2683$  (Dougherty et al., 2005).  
 322 Here we used spherical harmonic coefficients based on Voyager 2 spacecraft  
 323 derived data. This model includes a full order-3 internal field, ring current  
 324 and accounts for the oblateness of the planet, and uses a Saturn equato-  
 325 rial radius of 60,268 km. An ionospheric height of 1200 km was chosen for  
 326 this mapping, which is approximately the observed  $H_3^+$  density peak altitude  
 327 (Stallard et al., 2012), and is consistent with modeled  $H_3^+$  altitudes at mid-  
 328 latitude (Kim et al., 2014).

#### 330 4. Results and discussion

331 Owing to this dataset having the highest signal strength of  $\text{H}_3^+$  recorded  
 332 at mid latitudes on Saturn, we are able to see and use two spectral lines to  
 333 calculate column-averaged  $\text{H}_3^+$  temperatures, densities and radiative cooling  
 334 rates, allowing us to finally measure how ring rain affects upper-atmospheric  
 335 chemistry and energy balance. In Table 1 we present the results obtained by  
 336 fitting to Saturn’s local-noon  $\text{H}_3^+$  emissions, integrated between  $103^\circ$  -  $176^\circ$   
 337 CML. A total of eleven fits were obtained from pole to pole, with an ab-  
 338 sence of fits near the equator being due to a combination of low  $\text{H}_3^+$  signal to  
 339 noise and interference from the continuum reflection of sunlight by the rings.  
 340 These results are the first non-auroral ( $<70^\circ\text{N/S}$  latitude)  $\text{H}_3^+$  parameters to  
 341 ever be derived at Saturn, and so offer new insights into the thermal and  
 342 chemical modification of the ionosphere and co-located thermosphere by the  
 343 impinging ring rain phenomenon and other phenomena. The following re-  
 344 sults map mostly to features in the equatorial plane such as the A, B and C  
 345 subdivisions of the main rings, Saturn’s satellite’s Mimas and Enceladus, the  
 346 E-ring and the aurorae. In addition, a B/C ring boundary was also studied  
 347 due the expectation that it is a source of charged icy grains.

348  
 349 Figure 5 shows  $N_{\text{H}_3^+}$  and normalized inverse (stratospheric) haze opacity,  
 350  $\tau^{-1}$  taken from Connerney (1986), as a function latitude and radially mapped  
 351 distance. Connerney (1986) proposed that haze particles could act as con-  
 352 densation nuclei to the downward diffusing water, thus making haze particles  
 353 heavy enough to sink. Here we show the inverse haze opacity, which repre-  
 354 sents the degree to which the haze layer has become thinned (by ring rain): a  
 355 value of 0 means the haze layer is dense, while a value of 1 means the haze is  
 356 less dense. Densities of  $\text{H}_3^+$  are high near Saturn’s auroral regions, but reach  
 357 their highest point near the expected location of a ‘ring rain’ influx emanating  
 358 from the B- and C-rings. In the north, the results suggest that the inner-edge  
 359 of the B-ring is the largest source of icy grains. While the uncertainties are  
 360 large in the northern hemisphere, limiting our ability to draw definitive con-  
 361 clusions about the influence of rain there,  $39^\circ\text{S}$  was found to have a high  $N_{\text{H}_3^+}$ ,  
 362 with uncertainties mostly clear of those at adjacent latitudes. These peaks  
 363 in  $N_{\text{H}_3^+}$  most likely indicate that an influx of ring material (such as water) is  
 364 falling at these latitudes and removes electrons, which in turn increases the

Table 1: Saturn’s fitted  $\text{H}_3^+$  parameters as a function of planetocentric latitude (Lat PC) and corresponding magnetic field mapping out to the equatorial plane (Eq. Radius). Note that this mapping was evaluated at 1200 km altitude above Saturn’s 1-bar pressure surface. Parameter uncertainties shown are one standard deviation. The listed features are the approximate locations covered by each latitudinal swath.

Region	Lat PC	Eq. Radius ( $R_s$ )	Feature	$N(\text{H}_3^+)$ $10^{11} \text{ cm}^{-2}$	$T(\text{H}_3^+)$ Kelvin	$L(\text{H}_3^+)$ $10^{-6} \text{ Wm}^{-2} \text{ sr}^{-1}$
1	80 - 69°N	30.7 - 5.7	Aurora	$4.9 \pm 3.8$	$443 \pm 65$	$4.3 \pm 0.8$
2	69 - 60°N	5.7 - 2.97	Enceladus/E-ring	$1.0 \pm 0.6$	$515 \pm 58$	$4.1 \pm 0.6$
3	60 - 53°N	2.97 - 2.09	A-ring to Mimas	$5.3 \pm 4.5$	$424 \pm 69$	$2.6 \pm 0.5$
4	51 - 43°N	1.93 - 1.51	B-ring	$11.6 \pm 9.2$	$377 \pm 47$	$2.4 \pm 0.3$
5	47 - 43°N	1.69 - 1.51	B/C Boundary	$6.1 \pm 5.4$	$433 \pm 84$	$2.8 \pm 0.6$
6	26 - 37°S	1.25 - 1.52	C-ring	$1.1 \pm 0.8$	$544 \pm 96$	$4.6 \pm 1.2$
7	35 - 44°S	1.46 - 1.81	B/C Boundary	$24 \pm 16.5$	$348 \pm 31$	$2.9 \pm 0.2$
8	37 - 47°S	1.52 - 1.99	B-ring	$7.2 \pm 4.5$	$396 \pm 36$	$3.3 \pm 0.3$
9	47 - 57°S	2.0 - 2.9	A-ring to Mimas	$3.5 \pm 1.3$	$455 \pm 27$	$6.5 \pm 0.4$
10	57 - 67°S	2.9 - 5.8	Enceladus/E-ring	$5.2 \pm 1.2$	$479 \pm 17$	$15.5 \pm 0.7$
11	68 - 75°S	6.4 - 18.0	Aurora	$2.7 \pm 0.7$	$519 \pm 23$	$14.4 \pm 0.8$

<sup>365</sup>  $\text{H}_3^+$  density by mitigating the  $\text{H}_3^+$ -electron recombination rate (Moore et al.,  
<sup>366</sup> 2015). The highest density was observed in the southern hemisphere from  
<sup>367</sup> region 7, which is expected since the magnetic field permeating the rings is  
<sup>368</sup> inclined towards the south (Connerney, 1986). The low  $\text{H}_3^+$  density of region  
<sup>369</sup> 6 appears to be the result of an exceptionally high rain influx: we define  
<sup>370</sup> this area as an ‘overflow’ region, and it coincides with the thinnest region of  
<sup>371</sup> stratospheric haze. Indeed, Connerney (1986) predicted an influx near 38° S  
<sup>372</sup> of  $2 \times 10^9$  molecules  $\text{cm}^{-2} \text{ s}^{-1}$  which is in agreement with Moore et al. (2015),  
<sup>373</sup> who show that influxes greater than  $4 \times 10^8$  molecules  $\text{cm}^{-2} \text{ s}^{-1}$  are enough to  
<sup>374</sup> locally reduce  $N_{\text{H}_3^+}$  through charge-exchange between  $\text{H}_3^+$  and water, which  
<sup>375</sup> begins to overwhelm the enhancement in  $\text{H}_3^+$  given by the reduction in elec-  
<sup>376</sup> tron density.

<sup>377</sup>  
<sup>378</sup> The northern regions 4 and 5 have an average column-integrated  $\text{H}_3^+$  den-  
<sup>379</sup> sity of  $8.85 \pm 5.3 \times 10^{11} \text{ cm}^{-2}$ , which is consistent with a water product influx  
<sup>380</sup> of between  $7 \times 10^6$  and  $7 \times 10^7 \text{ cm}^{-2} \text{ s}^{-1}$ , according to Figure 4 of Moore et al.  
<sup>381</sup> (2015). This implies that regions 4 and 5 deliver  $27 \pm 22 \text{ kg s}^{-1}$  of water  
<sup>382</sup> products to the ionosphere, if the flow is deposited at all longitudes. For re-  
<sup>383</sup> gions 7 and 8, the average  $\text{H}_3^+$  density of  $15.6 \pm 8.5 \times 10^{11} \text{ cm}^{-2}$  implies a water



384 product influx of  $14 \pm 7 \text{ kg s}^{-1}$ . To explain the  $\text{H}_3^+$  density range of region 6,  
 385 a water product flow rate of either near  $4 \times 10^5 \text{ molecules cm}^{-2} \text{ s}^{-1}$  or  $2 \times 10^9$   
 386  $\text{molecules cm}^{-2} \text{ s}^{-1}$  is required (Moore et al., 2015). Since the latter value is  
 387 what is predicted by Connerney and Waite (1984), we favor the higher rate  
 388 here and thus eliminate the problem of degeneracy for this region. An influx  
 389  $6 \times 10^8 - 4 \times 10^9 \text{ molecules cm}^{-2} \text{ s}^{-1}$  can explain the density range found in re-  
 390 gion 6 (Moore et al., 2015), which corresponds to  $420 - 2800 \text{ kg s}^{-1}$  of water  
 391 products entering the planet. In total, we estimate an influx of water prod-  
 392 ucts from Saturn’s rings to the planet, at the latitudes measured here, of  $432$   
 393  $- 2870 \text{ kg s}^{-1}$ . At this mass loss rate, and using a total mass of Saturn’s rings  
 394 of  $1.52 \times 10^{19} \text{ kg}$  (Voosen, 2017), the ring system has  $292^{+818}_{-124}$  million years  
 395 before it is completely consumed by the planet. This estimate of ring lifetime  
 396 has a number of assumptions: 1) that the ring system is able to disperse over  
 397 time (e.g. by micrometeoroid bombardment), allowing the C-ring to act as  
 398 a continually replenished source region; 2) we measured Saturn during the  
 399 conditions of northern Spring, so the values above do not yet account for how  
 400 Saturn’s ring rain influx may change with season; 3) equatorial losses were  
 401 not accounted for here (Perry et al., 2018; Waite et al., 2018), so the mass  
 402 loss rate and ring lifetime estimates above are upper limits based strictly on  
 403 a mid-latitude influx of water products alone.

404  
 405 Moore et al. (2015) estimated  $N_{\text{H}_3^+}$  from the observations of  $\text{H}_3^+ \text{ Q}(1,0^-)$   
 406 line emission taken by O’Donoghue et al. (2013), i.e. the same observations  
 407 reported here (e.g. see Figure 2), by assuming a range of  $T_{\text{H}_3^+}$  of  $\sim 430 - 500$   
 408 K in both hemispheres.  $\text{H}_3^+$  densities near  $39^\circ\text{S}$  were modeled to be  $1.8 - 3.2$   
 409  $\times 10^{11} \text{ cm}^{-2}$ , while those at  $45^\circ\text{N}$  were found to be range  $1.6 - 3 \times 10^{11} \text{ cm}^{-2}$   
 410 (Moore et al., 2015). By comparison, average densities of  $11.6 \pm 9.2 \times 10^{11}$   
 411  $\text{cm}^{-2}$  and  $24 \pm 16.5 \times 10^{11} \text{ cm}^{-2}$  were found near  $45^\circ\text{N}$  and  $39^\circ\text{S}$ , respectively,  
 412 were derived from our observations. The northern values are (within uncer-  
 413 tainties) in loose agreement with modeling, but the observed southern values  
 414 exceed the expected density. To explore why this is the case, we examine  
 415 the fitted values of  $T_{\text{H}_3^+}$  in Figure 6, which show temperatures of  $377 \pm 47$   
 416 K at  $45^\circ\text{N}$  and  $348 \pm 31 \text{ K}$  at  $39^\circ\text{S}$ . Since the observed intensity of a given  
 417  $\text{H}_3^+$  line depends linearly upon the ion’s density and exponentially on the  
 418 ion’s temperature (Melin et al., 2014), a model of  $\text{H}_3^+$  emission that uses an  
 419 overestimate of temperature will necessarily underestimate the ion’s density  
 420 (and vice versa). The modeled  $\text{H}_3^+$  densities will be larger at most latitudes

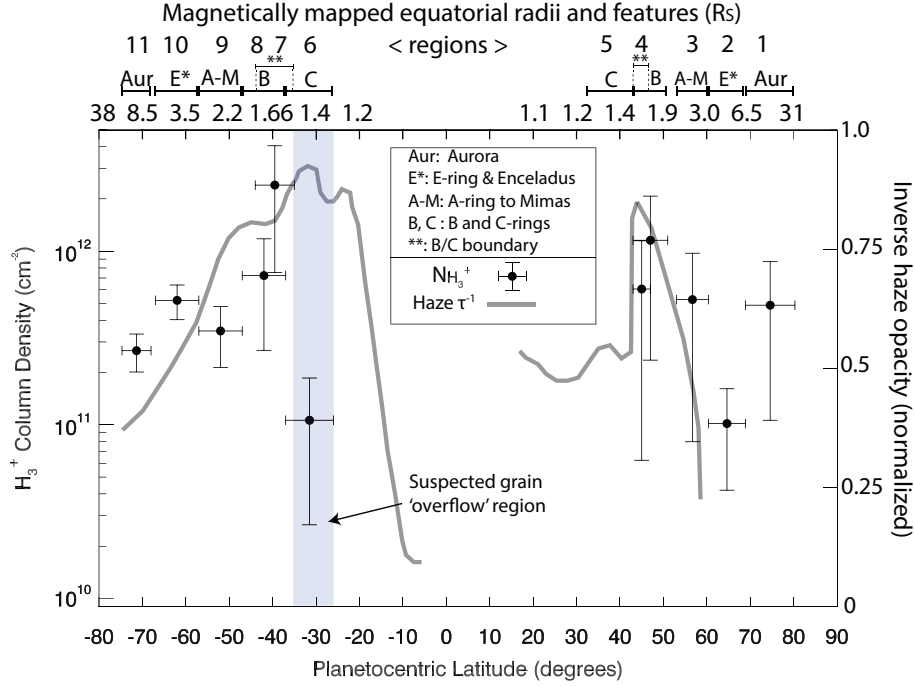


Figure 5: Saturn’s fitted  $\text{H}_3^+$  column densities,  $N_{\text{H}_3^+}$  and normalized inverse haze opacity,  $\tau^{-1}$ , as a function of planetocentric latitude and corresponding magnetic field mapping out to the equatorial plane,  $R_s$ . Latitudinal/radial ranges of each measurement are given by the horizontal lines on each value, while the density uncertainties (one standard deviation) are given by vertical lines. A blue-shaded region indicates the ‘overflow’ region where the largest influx of ring rain is expected ( $2 \times 10^9 \text{ molecules cm}^{-2} \text{ s}^{-1}$ ). The listed features are the approximate locations covered by each latitudinal swath.

421 in the model of Moore et al. (2015), provided that the observed temperatures  
 422 of 348 - 377 K are used instead of the previous 430 - 500 K (Luke Moore,  
 423 personal communication).

424

425 We will now consider how the altitudinal distribution of the ring rain  
 426 influx may give rise to an anti-correlation between  $T_{\text{H}_3^+}$  and  $N_{\text{H}_3^+}$  (the Spear-  
 427 man’s rank coefficient between these parameters is  $r = -0.93$ ). At 39°S, for  
 428 example, ring rain enters the upper atmosphere from space, and while diffus-  
 429 ing down to lower altitudes the grains will sublime (vaporize) according to  
 430 the speed and size of the grains (Moses and Poppe, 2017; Hamil et al., 2018).  
 431 The grain sizes and velocities derived from the Cassini CDA instrument data

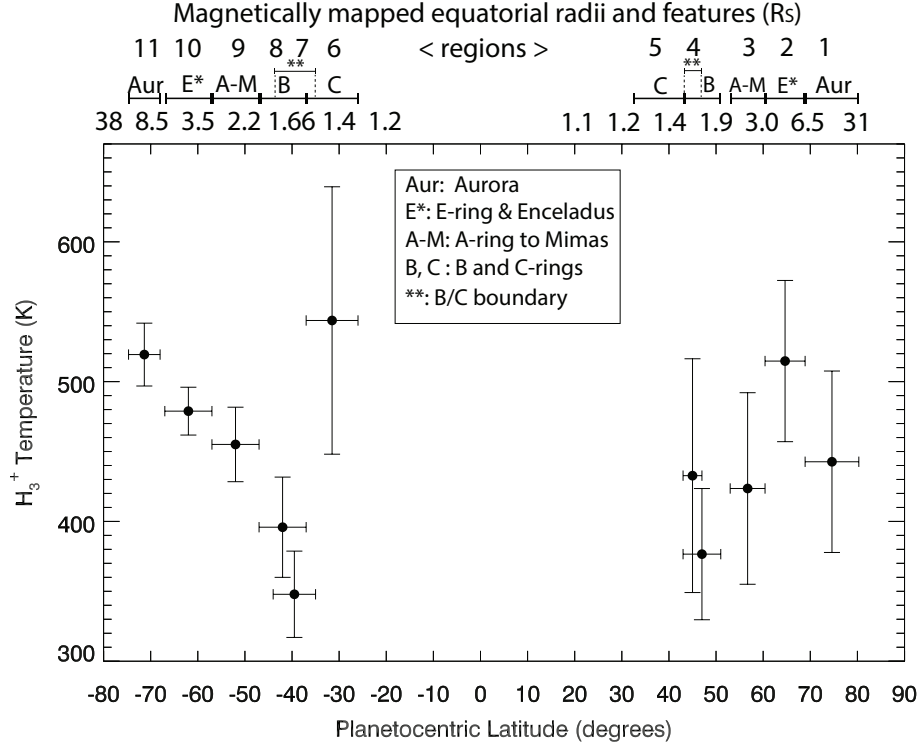


Figure 6: Saturn’s fitted  $\text{H}_3^+$  column averaged temperatures,  $T_{\text{H}_3^+}$ , as a function of planetocentric latitude and corresponding magnetic field mapping out to the equatorial plane,  $R_s$ . Latitudinal/radial ranges of each measurement are given by the horizontal lines on each value, while the temperature uncertainties (one standard deviation) are given by vertical lines. The listed features are the approximate locations covered by each latitudinal swath.

432 were generally found to be  $\sim 10$ s of nm in radius and have velocities of up to  
 433 several  $\text{km s}^{-1}$  (Hsu et al., 2018). According to the grain precipitation model  
 434 of Hamil et al. (2018), the nearest matching grain velocity/size for grains that  
 435 undergo significant sublimation are either  $15 \text{ km s}^{-1} / 100 \text{ nm}$  (which disin-  
 436 tegrate by 1085 km altitude) or  $25 \text{ km s}^{-1} / 10 \text{ nm}$  (1408 km final altitude).  
 437 When a photochemical model examined the release of a parcel of water in  
 438 Saturn’s atmosphere at 1750 km, it was found that the heaviest losses to  
 439 electron densities occur by altitudes of 1000 km (Moore and Mendillo, 2007).  
 440 We will assume (therefore) that chemical reactions between water products  
 441 and the atmosphere are most fervent near 1000 km, following sublimation  
 442 within the 1000 - 1500 km range (Moses and Poppe, 2017). With the addi-

tion of water products to lower altitudes, local electron densities would be reduced and consequently  $\text{H}_3^+$  ions would then have longer lifetimes, while the column-integrated emissions become more representative of the deeper, colder parts of the ionosphere (Moore et al., 2009; Tao et al., 2011). The high reported temperature in the south mapping to the C-ring may then be due to lower-atmospheric  $\text{H}_3^+$  being depleted by the aforementioned ‘overflow’ at lower latitudes, leaving primarily hotter/high-altitude upper-atmospheric  $\text{H}_3^+$  to be detected. A corresponding anti-correlation between  $N_{\text{H}_3^+}$  and  $T_{\text{H}_3^+}$  is also be present at  $45^\circ\text{N}$ , although the uncertainties in the region are too large to draw any definitive conclusions.

The mid-latitude temperatures reported here are mostly a few 10s Kelvin lower in temperature than those reported for the exosphere by Koskinen et al. (2015), an offset which was predicted by Moore et al. (2015). However, at latitudes pertaining to ring rain the temperatures are far lower, likely due to the anti-correlation effect described in the previous paragraph. The auroral/polar observations reported here were also analyzed by O’Donoghue et al. (2014), who compared and contrasted Saturn’s main auroral emissions in each hemisphere by summing the data between  $68 - 80^\circ$  north and south planetocentric latitude. Absence of Kronian-atmospheric windows (by methane absorption of sunlight) at the low latitudes led to only two  $\text{H}_3^+$  lines being usable in the present work, whereas five  $\text{H}_3^+$  lines were able to be used in the auroral regions of the previous study, leading to lower uncertainties. The northern  $\text{H}_3^+$  temperature and density was found to be  $527 \pm 18$  K and  $1.6 \times 10^{11} \pm 0.3 \text{ cm}^{-2}$ , while the southern parameters were  $583 \pm 13$  K and  $1.2 \times 10^{11} \pm 0.2 \text{ cm}^{-2}$ , respectively O’Donoghue et al. (2014). We mostly overlap these northern auroral latitudes and partially overlap the southern latitudes in this work (see Table 1), and see the same general results within uncertainties: that the southern aurorae of Saturn have hotter, less dense  $\text{H}_3^+$  than the northern aurorae. The northern auroral temperatures (region 1) are colder at  $443 \pm 65$  K, but this may be due to O’Donoghue et al. (2014) including 1 degree latitude more of region 2 than we do in the present paper.

The radiative cooling rate of  $\text{H}_3^+$ ,  $L_{\text{H}_3^+}$ , is shown in Figure 7 as a function of latitude. By far the largest output of radiation to space from  $\text{H}_3^+$  leaves from the southern auroral regions, a result that was also found at Saturn using Keck data in both 2011 and 2013 (O’Donoghue et al., 2014, 2016).

480 The pole-to-pole radiative cooling rate falls off towards the mid latitudes but  
 481 lingers particularly high near  $62^\circ\text{S}$ .  $L_{\text{H}_3^+}$  appears to be driven by relatively  
 482 high  $N_{\text{H}_3^+}$  as opposed to  $T_{\text{H}_3^+}$  in this region. Region 10, around  $62^\circ\text{S}$ , is of spe-  
 483 cial interest because a ‘second auroral oval’ of  $\text{H}_3^+$  was found at this location  
 484 by Stallard et al. (2008), followed by detection of the northern Enceladus  
 485 footprint in the UV (Pryor et al., 2011). This region maps to the icy moon  
 486 Enceladus which orbits at  $3.95 R_s$  (Tokar et al., 2008). Enceladus is a geo-  
 487 logically active body, outgassing neutral water products into a broad torus  
 488 which encircles Saturn, some of which becomes charged by photoionization  
 489 and charge-exchange (Johnson et al., 2006). A field-aligned current system  
 490 between Saturn and the Enceladus torus is thought to arise from this that  
 491 heats Saturn’s ionosphere, owing to ionospheric drag induced by accelerating  
 492 the charged part of the torus into co-rotation with the planet (Ray et al.,  
 493 2012). If charged water ions from the torus are able to flow into the iono-  
 494 sphere, they could have also caused the subtle rise in  $\text{H}_3^+$  density seen here  
 495 in a similar manner to ring rain. It is possible that both heating and ionized  
 496 water precipitation occur simultaneously, but our results hint that charged  
 497 water from Enceladus may be preferentially draining into Saturn’s southern  
 498 mid-latitudes. It is unclear why latitudes in the northern hemisphere associ-  
 499 ated with Enceladus do not also show a large  $\text{H}_3^+$  density.

500

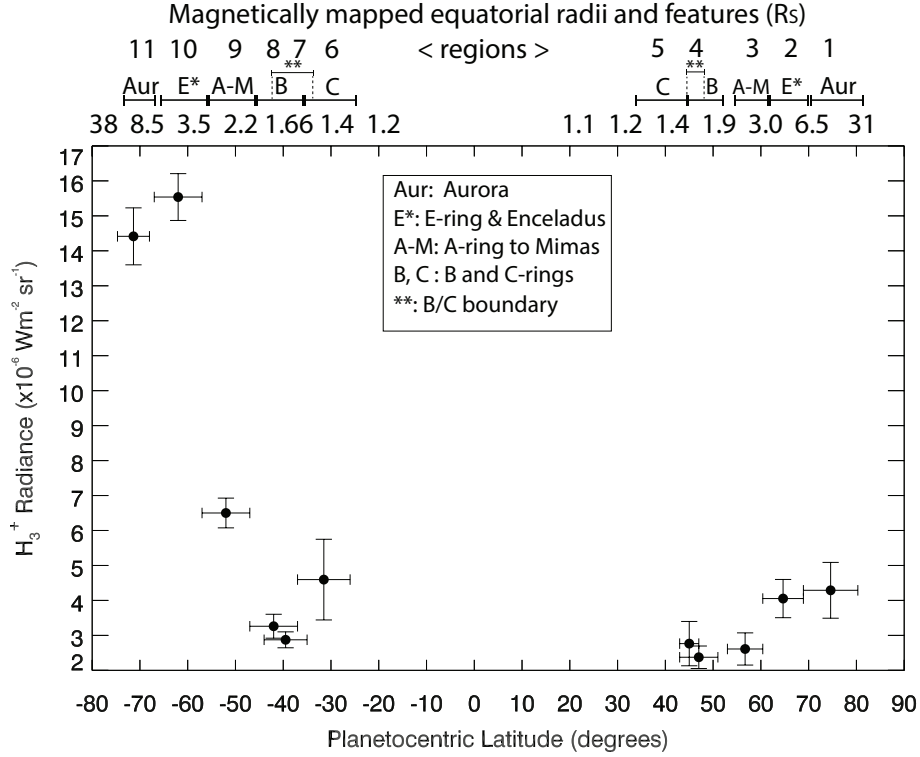


Figure 7: Saturn’s fitted  $H_3^+$  radiances (radiative cooling rates),  $L_{H_3^+}$ , as a function of planetocentric latitude and corresponding magnetic field mapping out to the equatorial plane,  $R_s$ . Latitudinal/radial ranges of each measurement are given by the horizontal lines on each value, while the radiance uncertainties (one standard deviation) are given by vertical lines. The listed features are the approximate locations covered by each latitudinal swath.

## 5. Conclusions

Ground-based observations of Saturn were obtained on 17 April 2011 using the 10-metre Keck telescope on Mauna Kea, Hawaii.  $H_3^+$  emissions were previously analyzed from these observations, showing peaks in emission at specific latitudes that correspond well with an expected influx of charged water products (O’Donoghue et al., 2013). Subsequent modeling showed that the larger emissions are most likely driven by an increase in  $H_3^+$  density (rather than temperature) relative to adjacent latitudes, and that this is facilitated by the removal of electrons which allow the  $H_3^+$  lifetime to be extended where the influx occurs (Moore et al., 2015). In this study we

511 performed a new analysis of the April 2011 data, successfully deriving the  
 512  $\text{H}_3^+$  parameters temperature, density and radiative cooling rates for the first  
 513 time at the non-auroral regions of Saturn. Until now, we have not had direct  
 514 evidence that  $\text{H}_3^+$  densities are driving the peaks in  $\text{H}_3^+$  emission. Our findings  
 515 are summarized below:

- 516 1. We find that  $\text{H}_3^+$  density is enhanced near  $45^\circ\text{N}$  and  $39^\circ\text{S}$  planetocen-  
 517 tric latitudes. An influx of ring material (probably water) causes the  
 518 enhancements seen through the chemical pathway described by Moore  
 519 et al. (2015).
- 520 2. The high  $\text{H}_3^+$  density at  $39^\circ\text{S}$  is due to the northward-offset magnetic  
 521 field in the vicinity of the ring plane, which leads to charged grains  
 522 being immediately drawn southwards due to gravitational forces in that  
 523 region (Connerney, 1986). Southern hemisphere mapping to the C-ring  
 524 shows low  $\text{H}_3^+$  density, likely due to the expected very large water influx  
 525 that begins to decrease  $\text{H}_3^+$  densities when charge-exchange between  
 526 with water and  $\text{H}_3^+$  begins to dominate (Moore et al., 2015). We define  
 527 this area as an ‘overflow region’.
- 528 3. We estimated the water product influx needed to explain the  $\text{H}_3^+$  densi-  
 529 ties by using previous modeling results (Moore et al., 2015). The rates  
 530 obtained were in agreement with the modeling work decades earlier by  
 531 Connerney and Waite (1984). The total water influx from the rings to  
 532 Saturn’s mid-latitude ionosphere inferred from the  $\text{H}_3^+$  measurements  
 533 herein is  $432 - 2870 \text{ kg s}^{-1}$ , values that would deplete the rings in  
 534  $292^{+818}_{-124}$  million years.
- 535 4. An anti-correlation between  $\text{H}_3^+$  temperature and density was observed.  
 536  $\text{H}_3^+$  temperatures were low while the density was high at  $39^\circ\text{S}$ , likely  
 537 indicating that the ionosphere is most affected by ring rain in the deep  
 538 ionosphere near 1200 km (Moore and Mendillo, 2007; Hamil et al.,  
 539 2018), as deeper precipitation necessarily weights the  $\text{H}_3^+$  density and  
 540 emissions to colder parts of the ionosphere (Moore et al., 2009; Tao  
 541 et al., 2011). In the region 6 ( $32^\circ \text{S}$ ) ‘overflow region’, this weighting  
 542 is reversed and high-altitude, warm  $\text{H}_3^+$  emission dominate, as low-  
 543 altitude  $\text{H}_3^+$  is expected to be completely depleted.
- 544 5. Saturn’s icy moon Enceladus appears to affect the mid-latitudes, with  
 545  $62^\circ\text{S}$  exhibiting relatively high  $\text{H}_3^+$  density compared to adjacent lati-  
 546 tudes. The results may indicate that charged water from Enceladus is  
 547 draining into Saturn’s southern mid-latitudes, though no corresponding

548 northern density peak was found.

549 **Acknowledgements** James O'Donoghue's research was supported by an  
550 appointment to the National Aeronautics and Space Administration (NASA)  
551 Postdoctoral Program at the NASA Goddard Space Flight Center, adminis-  
552 tered by Universities Space Research Association under contract with NASA.  
553 This material is based upon work supported by NASA under Grants NNX14AG72G  
554 and NNX17AF14G issued through the SSO Planetary Astronomy Program.  
555 The data presented herein were obtained at the W.M. Keck Observatory,  
556 which is Operated as a scientific partnership among the California Institute of  
557 Technology, the University of California, and NASA, and the data in the form  
558 of fits files are available from the Keck archive at <https://www2.keck.hawaii.edu/koa/public/koa.php>  
559 We are grateful to the staff at the Keck Observatory. The authors wish to  
560 recognize the significant cultural role and reverence that the summit of Mau-  
561 nakea has within the indigenous Hawaiian community: we are fortunate to  
562 have the opportunity to conduct observations from this mountain.

563 Atreya, S. K., Donahue, T. M., Nagy, A. F., Waite, Jr., J. H., McConnell,  
564 J. C., 1984. Theory, measurements, and models of the upper atmosphere  
565 and ionosphere of Saturn. University of Arizona Press, pp. 239–277.

566 Connerney, J., Apr. 2013. Solar system: Saturn's ring rain. *Nature* 496, 178–  
567 179.

568 Connerney, J. E. P., Aug. 1986. Magnetic connection for Saturn's rings and  
569 atmosphere. *Geophys. Res. Lett.* 13, 773–776.

570 Connerney, J. E. P., Ness, N. F., Acuna, M. H., Jul. 1982. Zonal harmonic  
571 model of Saturn's magnetic field from Voyager 1 and 2 observations. *Nature*  
572 298, 44–46.

573 Connerney, J. E. P., Waite, J. H., Nov. 1984. New model of Saturn's iono-  
574 sphere with an influx of water from the rings. *Nature* 312, 136–138.

575 Cuzzi, J., Clark, R., Filacchione, G., French, R., Johnson, R., Marouf,  
576 E., Spilker, L., 2009. Ring Particle Composition and Size Distribution.  
577 Springer, Dordrecht, p. 459.

578 Cuzzi, J. N., French, R. G., Hendrix, A. R., Olson, D. M., Roush, T., Vahi-  
579 dinia, S., Jul. 2018. HST-STIS spectra and the redness of Saturn's rings.  
580 *Icarus* 309, 363–388.



- 581 Dougherty, M. K., Achilleos, N., Andre, N., Arridge, C. S., Balogh, A.,  
582 Bertucci, C., Burton, M. E., Cowley, S. W. H., Erdos, G., Giampieri, G.,  
583 Glassmeier, K.-H., Khurana, K. K., Leisner, J., Neubauer, F. M., Russell,  
584 C. T., Smith, E. J., Southwood, D. J., Tsurutani, B. T., Feb. 2005. Cassini  
585 Magnetometer Observations During Saturn Orbit Insertion. *Science* 307,  
586 1266–1270.
- 587 Dougherty, M. K., Cao, H., Khurana, K. K., Hunt, G. J., Provan, G., Kellock,  
588 S., Burton, M. E., Burk, T. A., Bunce, E. J., Cowley, S. W. H., Kivelson,  
589 M. G., Russell, C. T., Southwood, D. J., 2018. Saturn’s magnetic field  
590 revealed by the cassini grand finale. *Science* 362 (6410).  
591 URL <http://science.sciencemag.org/content/362/6410/eaat5434>
- 592 Dougherty, M. K., Khurana, K. K., Neubauer, F. M., Russell, C. T., Saur,  
593 J., Leisner, J. S., Burton, M. E., Mar. 2006. Identification of a Dynamic  
594 Atmosphere at Enceladus with the Cassini Magnetometer. *Science* 311,  
595 1406–1409.
- 596 Hamil, O., Cravens, T. E., Reedy, N. L., Sakai, S., Feb. 2018. Fate of Ice  
597 Grains in Saturn’s Ionosphere. *J. Geophys. Res. (Space Physics)* 123, 1429–  
598 1440.
- 599 Hansen, C. J., Shemansky, D. E., Esposito, L. W., Stewart, A. I. F., Lewis,  
600 B. R., Colwell, J. E., Hendrix, A. R., West, R. A., Waite, Jr., J. H.,  
601 Teolis, B., Magee, B. A., Jun. 2011. The composition and structure of the  
602 Enceladus plume. *Geophys. Res. Lett.* 38, L11202.
- 603 Hsu, H.-W., Schmidt, J., Kempf, S., Postberg, F., Moragas-Klostermeyer,  
604 G., Seiß, M., Hoffmann, H., Burton, M., Ye, S., Kurth, W. S., Horányi,  
605 M., Khawaja, N., Spahn, F., Schirdehahn, D., O’Donoghue, J., Moore, L.,  
606 Cuzzi, J., Jones, G. H., Srama, R., 2018. In situ collection of dust grains  
607 falling from saturn’s rings into its atmosphere. *Science* 362 (6410).  
608 URL <http://science.sciencemag.org/content/362/6410/eaat3185>
- 609 Johnson, R. E., Melin, H., Stallard, T. S., Tao, C., Nichols, J. D., Chowd-  
610 hury, M. N., Jul. 2018. Mapping  $\text{H}_3^+$  Temperatures in Jupiter’s Northern  
611 Auroral Ionosphere Using VLT-CRIRES. *J. Geophys. Res. (Space Physics)*  
612 123, 5990–6008.

613 Johnson, R. E., Smith, H. T., Tucker, O. J., Liu, M., Burger, M. H., Sittler,  
614 E. C., Tokar, R. L., Jun. 2006. The Enceladus and OH Tori at Saturn.  
615 *Astrophys. J.* 644, L137–L139.

616 Kim, Y. H., Fox, J. L., Black, J. H., Moses, J. I., Jan. 2014. Hydrocarbon  
617 ions in the lower ionosphere of Saturn. *J. Geophys. Res. (Space Physics)*  
618 119, 384–395.

619 Kliore, A. J., Nagy, A., Asmar, S., Anabtawi, A., Barbinis, E., Fleischman,  
620 D., Kahan, D., Klose, J., Aug. 2014. The ionosphere of Saturn as observed  
621 by the Cassini Radio Science System. *Geophys. Res. Lett.* 41, 5778–5782.

622 Kliore, A. J., Patel, I. R., Lindal, G. F., Sweetnam, D. N., Hotz, H. B., Waite,  
623 J. H., McDonough, T., Nov. 1980. Structure of the ionosphere and atmo-  
624 sphere of Saturn from Pioneer 11 Saturn radio occultation. *J. Geophys.*  
625 *Res.* 85, 5857–5870.

626 Koskinen, T. T., Sandel, B. R., Yelle, R. V., Strobel, D. F., Müller-Wodarg,  
627 I. C. F., Erwin, J. T., Nov. 2015. Saturn’s variable thermosphere from  
628 Cassini/UVIS occultations. *Icarus* 260, 174–189.

629 Lam, H. A., Achilleos, N., Miller, S., Tennyson, J., Trafton, L. M., Geballe,  
630 T. R., Ballester, G. E., Jun. 1997. A Baseline Spectroscopic Study of the  
631 Infrared Auroras of Jupiter. *Icarus* 127, 379–393.

632 Liu, C.-M., Ip, W.-H., May 2014. A New Pathway of Saturnian Ring-  
633 Ionosphere Coupling via Charged Nanograins. *Astrophys. J.* 786, 34.

634 Markwardt, C. B., Sep. 2009. Non-linear Least-squares Fitting in IDL with  
635 MPFIT. In: Bohlender, D. A., Durand, D., Dowler, P. (Eds.), *Astronomi-  
636 cal Data Analysis Software and Systems XVIII*. Vol. 411 of *Astronomical  
637 Society of the Pacific Conference Series*. p. 251.

638 McElroy, M. B., Mar. 1973. The Ionospheres of the Major Planets (Article  
639 published in the *Space Science Reviews* special issue on ‘Outer Solar Sys-  
640 tem Exploration - An Overview’, ed. by J. E. Long and D. G. Rea.). *Space  
641 Sci. Rev.* 14, 460–473.

642 McLean, I. S., Becklin, E. E., Bendiksen, O., Brims, G., Canfield, J., Figer,  
643 D. F., Graham, J. R., Hare, J., Lacayanga, F., Larkin, J. E., Larson, S. B.,  
644 Levenson, N., Magnone, N., Teplitz, H., Wong, W., Aug. 1998. Design

645 and development of NIRSPEC: a near-infrared echelle spectrograph for  
646 the Keck II telescope. In: Fowler, A. M. (Ed.), Society of Photo-Optical  
647 Instrumentation Engineers (SPIE) Conference Series. Vol. 3354 of Society  
648 of Photo-Optical Instrumentation Engineers (SPIE) Conference Series. pp.  
649 566–578.

650 Melin, H., Stallard, T. S., Miller, S., Geballe, T. R., Trafton, L. M.,  
651 O’Donoghue, J., 2013. Post-equinoctial observations of the ionosphere of  
652 uranus. *Icarus* 223 (2), 741 – 748.

653 Melin, H., Stallard, T. S., O’Donoghue, J., Badman, S. V., Miller, S., Blake,  
654 J. S. D., Feb. 2014. On the anticorrelation between  $\text{H}_3^+$  temperature and  
655 density in giant planet ionospheres. *Mon. Not. R. Astron. Soc.* 438, 1611–  
656 1617.

657 Miller, S., Stallard, T., Melin, H., Tennyson, J., 2010.  $\text{H}_3^+$  cooling in planetary  
658 atmospheres. *Faraday Discussions* 147, 283–291.

659 Mitchell, D. G., Perry, M. E., Hamilton, D. C., Westlake, J. H., Kollmann,  
660 P., Smith, H. T., Carbary, J. F., Waite, J. H., Perryman, R., Hsu, H.-W.,  
661 Wahlund, J.-E., Morooka, M. W., Hadid, L. Z., Persoon, A. M., Kurth,  
662 W. S., 2018. Dust grains fall from saturn’s d-ring into its equatorial upper  
663 atmosphere. *Science* 362 (6410).  
664 URL <http://science.sciencemag.org/content/362/6410/eaat2236>

665 Moore, L., Galand, M., Mueller-Wodarg, I., Mendillo, M., Dec. 2009. Re-  
666 sponse of Saturn’s ionosphere to solar radiation: Testing parameterizations  
667 for thermal electron heating and secondary ionization processes. *Planetary*  
668 *and Space Science* 57, 1699–1705.

669 Moore, L., Mendillo, M., Jun. 2007. Are plasma depletions in Saturn’s iono-  
670 sphere a signature of time-dependent water input? *Geophys. Res. Lett.*  
671 34, 12202.

672 Moore, L., O’Donoghue, J., Müller-Wodarg, I., Galand, M., Mendillo, M.,  
673 Jan. 2015. Saturn ring rain: Model estimates of water influx into Saturn’s  
674 atmosphere. *Icarus* 245, 355–366.

675 Moses, J. I., Bass, S. F., Mar. 2000. The effects of external material on  
676 the chemistry and structure of Saturn’s ionosphere. *J. Geophys. Res.* 105,  
677 7013–7052.

678 Moses, J. I., Poppe, A. R., Nov. 2017. Dust ablation on the giant planets:  
679 Consequences for stratospheric photochemistry. *Icarus* 297, 33–58.

680 Neale, L., Miller, S., Tennyson, J., Jun. 1996. Spectroscopic Properties of the  
681  $\text{H}_3^+$  Molecule: A New Calculated Line List. *Astrophys. J.* 464, 516–520.

682 Nicholson, P. D., Hedman, M. M., Clark, R. N., Showalter, M. R., Cruik-  
683 shank, D. P., Cuzzi, J. N., Filacchione, G., Capaccioni, F., Cerroni, P.,  
684 Hansen, G. B., Sicardy, B., Drossart, P., Brown, R. H., Buratti, B. J.,  
685 Baines, K. H., Coradini, A., Jan. 2008. A close look at Saturn’s rings with  
686 Cassini VIMS. *Icarus* 193, 182–212.

687 Northrop, T. G., Connerney, J. E. P., Apr. 1987. A micrometeorite erosion  
688 model and the age of Saturn’s rings. *Icarus* 70, 124–137.

689 Northrop, T. G., Hill, J. R., Aug. 1982. Stability of negatively charged dust  
690 grains in Saturn’s ring plane. *J. Geophys. Res.* 87, 6045–6051.

691 Northrop, T. G., Hill, J. R., Aug. 1983. The inner edge of Saturn’s B ring.  
692 *J. Geophys. Res.* 88, 6102–6108.

693 O’Donoghue, J., Melin, H., Stallard, T. S., Provan, G., Moore, L., Badman,  
694 S. V., Cowley, S. W. H., Baines, K. H., Miller, S., Blake, J. S. D., Jan.  
695 2016. Ground-based observations of Saturn’s auroral ionosphere over three  
696 days: Trends in  $\text{H}_3^+$  temperature, density and emission with Saturn local  
697 time and planetary period oscillation. *Icarus* 263, 44–55.

698 O’Donoghue, J., Moore, L., Connerney, J. E. P., Melin, H., Stallard, T. S.,  
699 Miller, S., Baines, K. H., Dec. 2017. Redetection of the Ionospheric  $\text{H}_3^+$   
700 Signature of Saturn’s “Ring Rain”. *Geophys. Res. Lett.* 44, 11.

701 O’Donoghue, J., Stallard, T. S., Melin, H., Cowley, S. W. H., Badman, S. V.,  
702 Moore, L., Miller, S., Tao, C., Baines, K. H., Blake, J. S. D., Feb. 2014.  
703 Conjugate observations of Saturn’s northern and southern  $\text{H}_3^+$  aurorae.  
704 *Icarus* 229, 214–220.

705 O’Donoghue, J., Stallard, T. S., Melin, H., Jones, G. H., Cowley, S. W. H.,  
706 Miller, S., Baines, K. H., Blake, J. S. D., Apr. 2013. The domination of  
707 Saturn’s low-latitude ionosphere by ring ‘rain’. *Nature* 496, 193–195.

708 Perry, M., Waite Jr, J., Mitchell, D., Miller, K., Cravens, T., Perryman, R.,  
709 Moore, L., Yelle, R., Hsu, H.-W., Hedman, M., et al., 2018. Material flux  
710 from the rings of saturn into its atmosphere. *Geophys. Res. Lett.*

711 Prangé, R., Fouchet, T., Courtin, R., Connerney, J. E. P., McConnell, J. C.,  
712 Feb. 2006. Latitudinal variation of Saturn photochemistry deduced from  
713 spatially-resolved ultraviolet spectra. *Icarus* 180, 379–392.

714 Pryor, W. R., Rymer, A. M., Mitchell, D. G., Hill, T. W., Young, D. T.,  
715 Saur, J., Jones, G. H., Jacobsen, S., Cowley, S. W. H., Mauk, B. H.,  
716 Coates, A. J., Gustin, J., Grodent, D., Gérard, J.-C., Lamy, L., Nichols,  
717 J. D., Krimigis, S. M., Esposito, L. W., Dougherty, M. K., Jouchoux,  
718 A. J., Stewart, A. I. F., McClintock, W. E., Holsclaw, G. M., Ajello, J. M.,  
719 Colwell, J. E., Hendrix, A. R., Crary, F. J., Clarke, J. T., Zhou, X., Apr.  
720 2011. The auroral footprint of Enceladus on Saturn. *Nature* 472, 331–333.

721 Ray, L. C., Galand, M., Moore, L. E., Fleshman, B. L., Jul. 2012. Charac-  
722 terizing the limitations to the coupling between Saturn’s ionosphere and  
723 middle magnetosphere. *J. Geophys. Res. (Space Physics)* 117, A07210.

724 Srama, R., Ahrens, T. J., Altobelli, N., Auer, S., Bradley, J. G., Burton,  
725 M., Dikarev, V. V., Economou, T., Fechtig, H., Görlich, M., Grande, M.,  
726 Graps, A., Grün, E., Havnes, O., Helfert, S., Horanyi, M., Igenbergs, E.,  
727 Jessberger, E. K., Johnson, T. V., Kempf, S., Krivov, A. V., Krüger,  
728 H., Mocker-Ahlreep, A., Moragas-Klostermeyer, G., Lamy, P., Landgraf,  
729 M., Linkert, D., Linkert, G., Lura, F., McDonnell, J. A. M., Möhlmann,  
730 D., Morfill, G. E., Müller, M., Roy, M., Schäfer, G., Schlotzhauer, G.,  
731 Schwehm, G. H., Spahn, F., Stübiger, M., Svestka, J., Tschernjawski, V.,  
732 Tuzzolino, A. J., Wäsch, R., Zook, H. A., Sep. 2004. The Cassini Cosmic  
733 Dust Analyzer. *Space Sci. Rev.* 114, 465–518.

734 Stallard, T., Miller, S., Melin, H., Lystrup, M., Cowley, S. W. H., Bunce,  
735 E. J., Achilleos, N., Dougherty, M., Jun. 2008. Jovian-like aurorae on  
736 Saturn. *Nature* 453, 1083–1085.

737 Stallard, T. S., Melin, H., Miller, S., Badman, S. V., Baines, K. H., Brown,  
738 R. H., Blake, J. S. D., O’Donoghue, J., Johnson, R. E., Bools, B., Pilk-  
739 ington, N. M., East, O. T. L., Fletcher, M., Aug. 2015. Cassini VIMS  
740 observations of  $\text{H}_3^+$  emission on the nightside of Jupiter. *J. Geophys. Res.*  
741 (Space Physics) 120, 6948–6973.

742 Stallard, T. S., Melin, H., Miller, S., O' Donoghue, J., Cowley, S. W. H.,  
743 Badman, S., Adriani, A., Brown, R. H., Baines, K. H., Oct. 2012. Tem-  
744 perature changes and energy inputs in giant planet atmospheres: what we  
745 are learning from  $\text{H}_3^+$ . *Phil. Trans. Roy. Soc.* 370, 5213–5224.

746 Tao, C., Badman, S. V., Fujimoto, M., Jun. 2011. UV and IR auroral emission  
747 model for the outer planets: Jupiter and Saturn comparison. *Icarus* 213,  
748 581–592.

749 Tokar, R. L., Wilson, R. J., Johnson, R. E., Henderson, M. G., Thomsen,  
750 M. F., Cowee, M. M., Sittler, E. C., Young, D. T., Crary, F. J., McAn-  
751 dreds, H. J., Smith, H. T., Jul. 2008. Cassini detection of water-group  
752 pick-up ions in the Enceladus torus. *Geophys. Res. Lett.* 35, 14202.

753 Voosen, P., Dec. 2017. Saturn's rings are solar system newcomers. *Science*  
754 358, 1513–1514.

755 Waite, J. H., Atreya, S. K., Nagy, A. F., Sep. 1979. The ionosphere of Saturn  
756 - Predictions for Pioneer 11. *Geophys. Res. Lett.* 6, 723–726.

757 Waite, J. H., Perryman, R. S., Perry, M. E., Miller, K. E., Bell, J., Cravens,  
758 T. E., Glein, C. R., Grimes, J., Hedman, M., Cuzzi, J., Brockwell, T.,  
759 Teolis, B., Moore, L., Mitchell, D. G., Persoon, A., Kurth, W. S., Wahlund,  
760 J.-E., Morooka, M., Hadid, L. Z., Chocron, S., Walker, J., Nagy, A., Yelle,  
761 R., Ledvina, S., Johnson, R., Tseng, W., Tucker, O. J., Ip, W.-H., 2018.  
762 Chemical interactions between saturn's atmosphere and its rings. *Science*  
763 362 (6410).  
764 URL <http://science.sciencemag.org/content/362/6410/eaat2382>

765 Zebker, H. A., Marouf, E. A., Tyler, G. L., Dec. 1985. Saturn's rings - Particle  
766 size distributions for thin layer model. *Icarus* 64, 531–548.